UC Irvine
UC Irvine Previously Published Works

Title
Resonant acoustic radiation force optical coherence elastography

Permalink
https://escholarship.org/uc/item/2w93h8ft

Journal
Applied Physics Letters, 103(10)

ISSN
0003-6951

Authors
Qi, Wenjuan
Li, Rui
Ma, Teng
et al.

Publication Date
2013-09-02

DOI
10.1063/1.4820252

Peer reviewed

eScholarship.org Powered by the California Digital Library
University of California

Resonant acoustic radiation force optical coherence elastography

Wenjuan Qi,[1,2,a)] Rui Li,[1,a)] Teng Ma,[3] Jiawen Li,[1,4] K. Kirk Shung,[3] Qifa Zhou,[3] and Zhongping Chen[1,2,4]
[1]*Beckman Laser Institute, University of California Irvine, 1002 Health Sciences Road East, Irvine, California 92612, USA*
[2]*Department of Chemical Engineering and Materials Science, University of California Irvine, Irvine, California 92697, USA*
[3]*Department of Biomedical Engineering, NIH Ultrasonic Transducer Resource Center, University of Southern California, Los Angeles, California 90089, USA*
[4]*Department of Biomedical Engineering, University of California Irvine, Irvine, California 92697, USA*

(Received 14 June 2013; accepted 21 August 2013; published online 6 September 2013)

We report on a resonant acoustic radiation force optical coherence elastography (ARF-OCE) technique that uses mechanical resonant frequency to characterize and identify tissues of different types. The linear dependency of the resonant frequency on the square root of Young's modulus was validated on silicone phantoms. Both the frequency response spectrum and the 3D imaging results from the agar phantoms with hard inclusions confirmed the feasibility of deploying the resonant frequency as a mechanical contrast for tissue imaging. Furthermore, the results of resonant ARF-OCE imaging of a post-mortem human coronary artery with atherosclerosis demonstrate the potential of the resonant ARF-OCE as a non-invasive method for imaging and characterizing vulnerable plaques.
© *2013 AIP Publishing LLC*. [http://dx.doi.org/10.1063/1.4820252]

Knowledge of tissue mechanical properties provides valuable medical information in disease diagnosis and prognosis. There is a close correlation between tissue elasticity and pathology. For example, in atherosclerosis, measurement of tissue biomechanical properties has the potential to differentiate between various plaque components. Furthermore, tissue mechanical properties provide critical information to assess the vulnerability of plaques.[1–5] The stress in the cap increases with decreasing thickness and increasing macrophage infiltration. High strain locations in the vessel wall indicate the presence of vulnerable plaques.[1–4]

The mechanical resonant frequency of material in response to an external force is closely related to its elastic properties. The resonance frequency measurement techniques, such as resonant ultrasound spectroscopy, have been employed for decades to assess the elastic moduli in nondestructive evaluation of materials with a known shape.[6] Realizing that biological samples also exhibit mechanical resonance inherent to the samples, investigators have developed a variety of resonance frequency imaging techniques to evaluate the corresponding elastic moduli.[6–11] However, these existing techniques have limited sensitivity and are difficult to adapt for *in vivo* imaging. Recently, we developed a phase-resolved acoustic radiation force optical coherence elastography (ARF-OCE) system that uses an amplitude modulated (AM) acoustic wave to apply dynamic pressure to the tissue and uses phase-resolved optical coherence tomography (OCT) to evaluate the elastic properties of vascular tissue.[12] The phase-resolved ARF-OCE combines the high-speed excitation of ARF with sub-micrometer/nanometer detection sensitivity of phase-resolved OCT to achieve high speed and high sensitivity mapping of elastic properties of tissue, which has great potential for clinical cardiovascular imaging. However, while the relative value of strain and Young's module can be imaged with ARF-OCE, the absolute determination of these biomechanical properties requires knowledge of ARF applied to the tissue. Although ARF can be determined by simulation and calibration, adoption for *in vivo* quantification with constant change in geometry will be a significant challenge. In this paper, we report on a resonant phase-resolved ARF-OCE technique utilizing mechanical resonant frequency to image and quantify tissue mechanical parameters without knowledge of ARF parameters. Using the ARF as excitation allows us to sweep different ARF frequencies and measure the frequency dependent displacement in order to determine tissue resonance frequency, which can be used to image and quantify tissue mechanical properties.

The resonant ARF-OCE imaging was performed using an 890 nm spectral-domain OCT system, as shown in Figure 1, which was similar to the one described in an earlier work.[12] The acoustic radiation force was generated by a focused ultrasound transducer, which generated a 4 MHz ultrasound wave with a lateral focal width of 2.3 mm and a length of 18 mm at around a 60 mm working distance. A RF power amplifier, with a linear gain of 46 dB between 0.15 MHz and 230 MHz, amplified the signals driving the transducer. To create a cyclic acoustic radiation force, the ultrasound transducer was driven by a signal that was AM by a square wave. A function generator and a pulse delay generator were used to create the AM waveform, which, after power amplification, drove the ultrasound transducer. The pulse delay generator generated a low kHz square wave (50% duty cycle AM) which modulated the amplitude of the 4 MHz burst generated by the function generator. Different AM modulation frequencies were chosen to match with the resonances of phantoms and biological samples used in this paper. The modulation frequency and amplitude were chosen

[a)]W. Qi and R. Li contributed equally in this work.

 © 2013 AIP Publishing LLC

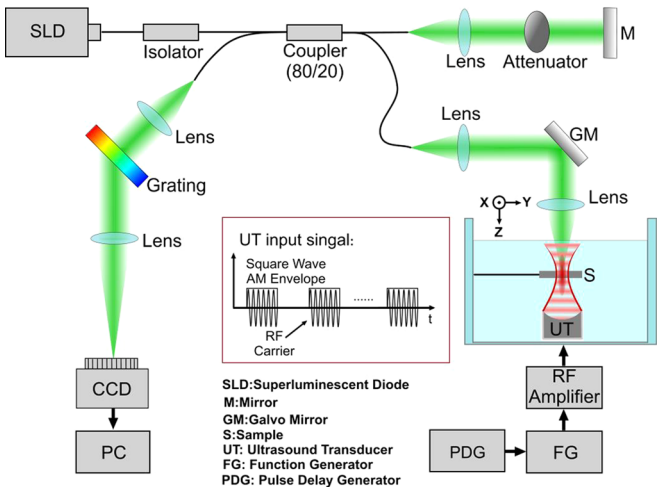

FIG. 1. Experimental setup.

for each sample in such a way that the absolute value of the phase difference induced between adjacent A-lines was large enough to enhance the sensitivity but less than $|\pi|$ to avoid phase wrapping. For all the experiment imaging, the samples were positioned in such plane that a relatively large area of uniform ARF induced displacement can be obtained. Experiment from homogeneous phantom confirmed that the ARF induced displacement is uniform over a 3.5×3.5 mm area, as shown in Figure 2. The local vibration phase of the sample was detected by a phase-resolved OCT system, which is capable of imaging at 20 kHz with a 3.5 μm axial resolution. The phase sensitivity was measured to be 1.5 mrad, thus, yielding nanometer sensitivity in terms of displacement.

Biological solid soft tissues, behaving intermediately between liquid and solid-elastic materials, are considered as viscoelastic materials, which usually can be described by the Voigt model.[13] This model is composed of a combination of a linear spring with an elastic constant k and a dashpot with a coefficient of viscosity γ. Under external force stimulation, this model can be described by[14]

$$m\ddot{z}(t) + \gamma\dot{z}(t) + kz(t) = F(t), \tag{1}$$

where m is the mass of the sample, $z(t)$ is the local displacement of the sample, and $F(t)$ is the acoustic radiation force exerted on the sample. When the deformation is small ($<0.1\%$), the elastic constants of soft tissues can be assumed to be linear.[15] Given the displacement of the sample, one can determine γ and k and thus solves the Young's modulus under Hook's law

$$E = kL/A = (\omega^2 + \lambda^2)mL/S, \tag{2}$$

where L and A are the thickness and area of the sample, respectively. The damping coefficient λ is defined as[14]

$$\lambda = -\gamma/2m. \tag{3}$$

For a defined material, the damping coefficient is constant. Therefore, there exists a linear relationship between the square root of the modulus and the resonant frequency of the sample with a fixed geometry.

To test this linear relationship, several homogeneous-cylindrical phantoms with a diameter of 35 mm and a height of 3 mm were made with different ratios of silicone to the corresponding activator for different Young's moduli. The frequency responses of silicone phantoms with varying Young's moduli were measured using our resonant ARF-OCE method by applying step frequency excitations. Figure 3 shows the linear dependency of Young's modulus of the material on the square of resonant frequency with an R^2 coefficient closes to 1, confirming the linear relationship and showing the potential for utilizing resonant frequency to differentiate materials with varying stiffness.

To demonstrate the mechanical contrast of the resonant ARF-OCE method, we first tested an agar phantom (0.8% agar, mass concentration and 0.4% intralipid, volumetric concentration) with a 513 μm metal ball embedded inside. For all experiments, the acoustic wave was applied perpendicular to the surface of the metal ball from the bottom of the water tank while the optical beam was applied perpendicularly from the top. The measured frequency response spectrogram of agar and metal ball was plotted in Figure 4. With different vibrational amplitudes due to significant elastic property differences, very strong resonances at 60 Hz and 1080 Hz were observed for the agar and stainless steel ball, respectively. This indicated that if a driving frequency of 1080 Hz were to be applied to the sample, one should be able to differentiate the stainless steel ball from the surrounding agar. We imaged the agar phantom under a modulation frequency of 1080 Hz, which was the resonant frequency of the

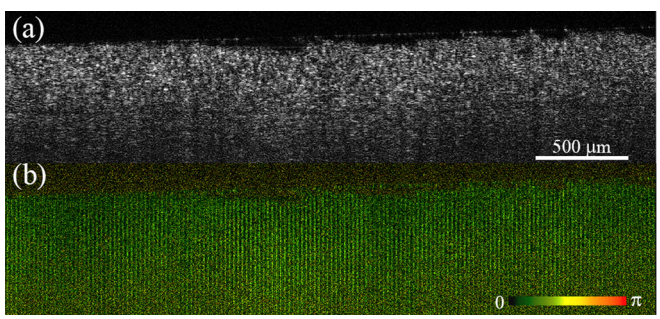

FIG. 2. OCT (a) and OCE (b) imaging for a homogeneous phantom. The ARF-induced displacement is confirmed to be uniform within the area scanned.

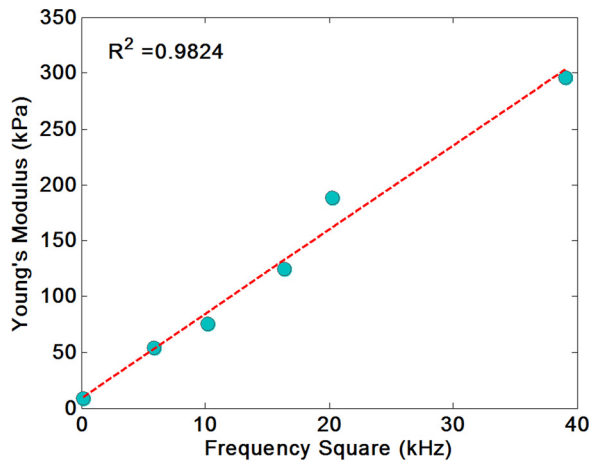

FIG. 3. Linear dependency curve of resonant frequencies on varying Young's moduli of silicone tissue phantoms.

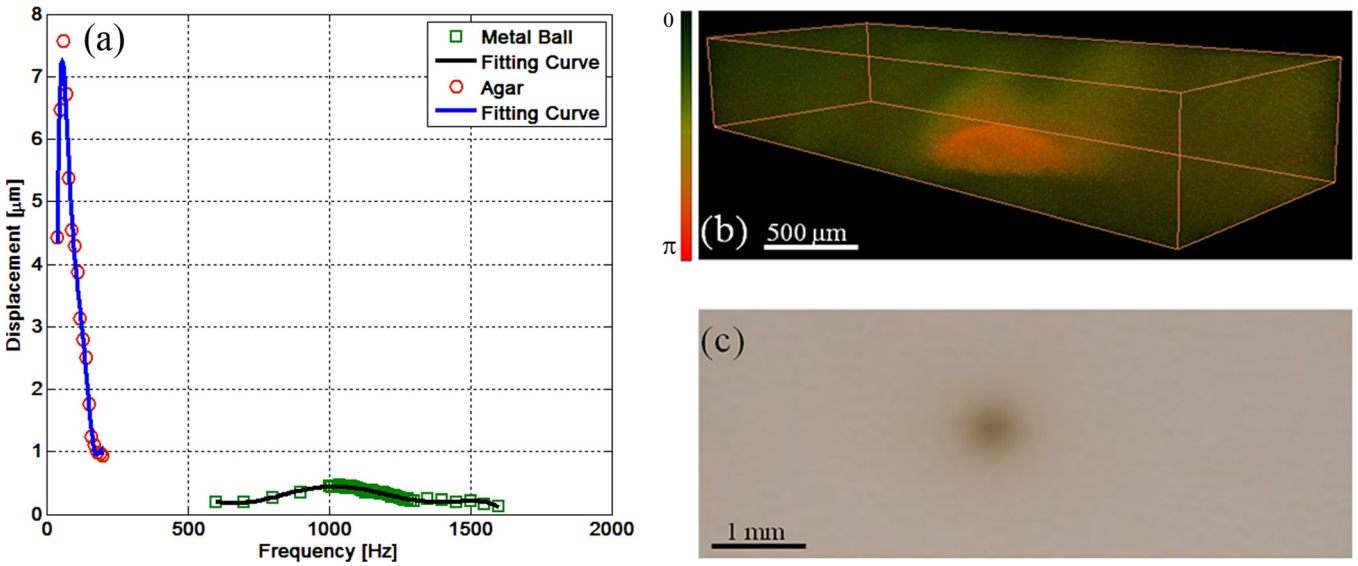

FIG. 4. (a) Frequency response spectrogram of agar and metal ball. M-mode vibration phase amplitude was recorded while the targeting point was stimulated by amplitude modulated acoustic radiation force. The modulation frequency was swept over a range of 50 Hz to 1600 Hz, covering the resonant frequency of both materials. The resonant frequency of agar and metal ball were 60 Hz and 1080 Hz, respectively. (b) 3D OCE image. (c) The sample image.

stainless steel ball. As expected, the metal ball produced a distinctive vibration amplitude in comparison with the surrounding agar, yielding high-contrast in the resonant elastography map (Figure 4(b)). Only the top of the metal ball can be seen in the images due to the highly reflective nature of the metal ball. The measured resonant frequency of the metal ball is not only related to the material but also affected by the size and shape of the metal ball.

We then tested the resonant ARF-OCE method on an agar phantom with a piece of silicone embedded inside. Silicone is stiffer than the surrounded agar but has similar optical properties as the agar. We imaged the agar phantom under a modulation frequency of 1250 Hz, which is around the resonant frequency of the embedded silicone. As expected, the silicone piece is barely discernable in the OCT image as shown in Figure 5(a). However, the silicone piece produced a distinctive vibration amplitude in comparison with the surrounding agar, yielding high-contrast in the resonant elastography map as shown in Figure 5(b). The fused OCT and OCE image is shown in Figure 5(c). These results again demonstrate that our resonant ARF-OCE can provide a strong mechanical contrast based on the resonant frequency of the material.

Finally, to test the feasibility of applying this resonant ARF-OCE technique to image and differentiate atherosclerotic plaques, *ex vivo* resonant ARF-OCE imaging of a section of post-mortem human coronary artery with atherosclerotic plaques was performed at varying frequencies. The human coronary artery was cut open, flattened, and preserved in saline solution prior to the experiment to keep it well hydrated. During the experiment, the human coronary was immersed in phosphate-buffered saline (PBS) solution, which served as both the coupling media for the ultrasonic wave and also the bio-environment for the tissue, and laterally scanned 3.5 mm where the vibration of the sample induced by the acoustic radiation force was evenly distributed. After ARF-OCE imaging, the sample was fixed using 10% formalin solution and sectioned for histological analysis. The histological sections were interpreted by a pathologist who had no access to the information provided by the resonant ARF-OCE method. The processed sample histology (Figures 6(d) and 6(e)) was confirmed as a necrotic core fibroatheroma (NCFA) with a fibrous cap, pointed by black arrows, on top of a necrotic lipid core (NC). Regions I and II of the fibrous cap are thin loose fibrous tissues ($\sim$100 μm thickness), where the plaque is more likely to rupture. In region III, the fibrous tissue becomes thicker and denser, which is considered as the stable area of the plaque. Tiny microscopic nodules of calcium salts were found at the boundary between the lipid core and the fibrous cap. The structure of the NCFA was reconstructed in the OCT image (Figure 6(a)), due to the limited penetration depth; only the fibrous cap and part of the lipid core can be seen in the OCT image. The structure revealed in the OCT image corresponded really

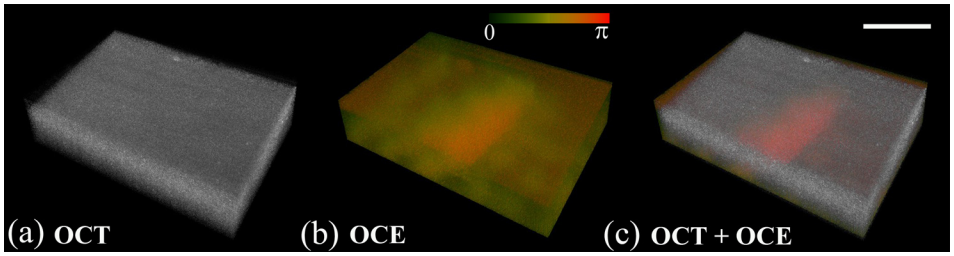

FIG. 5. OCT structural (a), resonant ARF-OCE (b), and fused images of agar phantom with a piece of silicone embedded inside (c) stimulated at a fixed frequency of 1250 Hz. The silicone shows distinctive vibration amplitude due to its resonance. The agar phantom, however, vibrates much less since the driving frequency is far away from its resonant frequency. Scale bar: 500 μm.

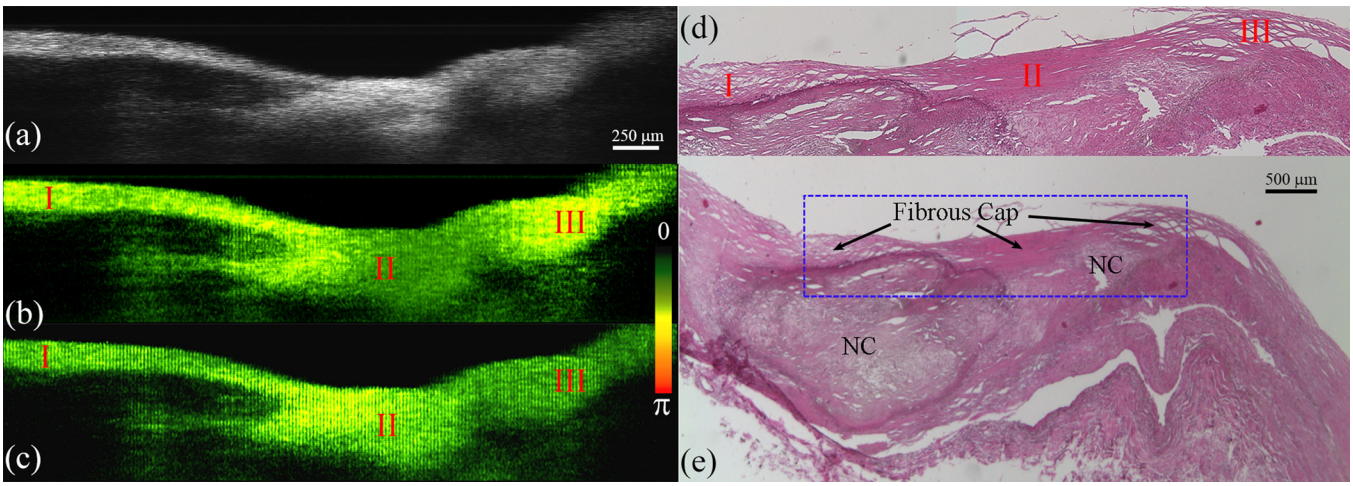

FIG. 6. Frequency response of human coronary artery. (a) OCT morphological image of the coronary artery segment in the dotted area in (e). (b) and (c) Resonant-ARF-OCE images showing frequency response at 500 Hz and 800 Hz. A higher vibration amplitude is measured on the left and right side of the resonant-ARF-OCE image (b) at 500 Hz, corresponding to the thin loose fibrous cap. High vibration is detected at 800 Hz at the center of the NCFA (c) corresponding to a thicker and denser portion of the fibrous cap. (c) and (d) Histological sections showing a NCFA with a fibrous cap (arrows) overlying a large NC. (e) Close-up view of the scanned area of plaque (dotted area in (e)).

well with the histological sections (Figure 6(d)). The resonant ARF-OCE distinguished different components in the plaque at varying frequencies. The thin, loose fibrous cap (regions I and II) showed higher resonant amplitude at a 500 Hz driving frequency (Figure 6(b)), as opposed to the thick, dense fibrous cap (region III) which showed very weak vibration at this frequency. Conversely, when the sample was excited under 800 Hz, the thick, dense fibrous cap portion started to show a stronger motion than the portion with the thin, loose fibrous cap. In Figure 6(c), the left part of the thin fibrous cap shows higher vibration than the one on the right side of the image. This may be a result of the calcium salts deposit on the left of the plaque, where higher reflection for the acoustic radiation force induced a relative stronger vibration than in the area without microscopic calcium nodules. Since the mechanical characteristics of the fibrous cap determines the stability of the plaque, the resonant-ARF-OCE method could provide useful mechanical information about the fibrous cap and thus may serve as a predictor of atherosclerotic plaque stability and provide useful information during clinical interventions, such as stent and balloon catheter insertion.

In summary, we have presented a resonant ARF-OCE technique, which takes advantage of the fact that materials respond primarily at their mechanical resonant frequencies, to effectively distinguish samples with varying stiffness. This method provides a significant contrast to a previously reported acoustic radiation force optical coherence elastography technique.[12] Resonant frequencies of silicone phantoms with different Young's moduli were investigated first with a focused ultrasound transducer that generated local acoustic radiation force stimulation at step-driven frequencies on the phantoms. A well-fitted linear dependency curve of the resonant frequency square on the Young's modulus was presented and thus validated the hypothesis of the method. The feasibility of this method on differentiating materials with different stiffness was tested on an agar phantom with a hard inclusion. Both the frequency response spectrum and the imaging results demonstrate the effectiveness of identifying the isolated hard inclusion by means of stimulating the sample at the resonant frequency. To demonstrate the potential of the resonant ARF-OCE technique for medical diagnosis and prognosis, we further performed resonant ARF-OCE measurement on a section of post-mortem human coronary artery with atherosclerotic plaques. A 2D OCT-structural image and phase resolved OCE maps were presented and correlated with a histological image. The phase resolved OCE maps identified regions of thin, loose and thick, dense fibrous caps with excitation frequencies of 500 Hz and 800 Hz, respectively. Although our current experiment uses the step-driven frequency scanning mechanism with limited imaging speed, the application of a chirped ultrasound signal to generate a frequency sweep ARF will significantly increase the imaging speed. The resonant ARF-OCE has great potential for intravascular *in vivo* imaging of atherosclerotic lesions where biomechanical properties of different types of plaques can be mapped.

The authors thank Ms. Claire Robertson for the mechanical test, and the individuals who donated their bodies and tissues for the advancement of education and research. This work was supported by the National Institutes of Health (R01EB-10090, R01EY-021519, R01HL-105215, R01HL-103764, and P41EB-015890), Air Force Office of Scientific Research (FA9550-04-0101), and the Arnold and Mabel Beckman Foundation. Dr. Chen has a financial interest in OCT Medical Inc., which, however, did not support this work.

[1]R. A. Baldewsing, J. A. Schaar, C. L. de Korte, F. Mastik, P. W. Serruys, and A. F. van der Steen, Stud. Health Technol. Inform. **113**, 75–96 (2005).
[2]C. L. de Korte and A. F. W. van der Steen, Ultrasonics **40**(1–8), 859–865 (2002).
[3]C. L. de Korte, M. J. Sierevogel, F. Mastik, C. Strijder, J. A. Schaar, E. Velema, G. Pasterkamp, P. W. Serruys, and A. F. van der Steen, Circulation **105**(14), 1627–1630 (2002).
[4]J. D. Allen, K. L. Ham, D. M. Dumont, B. Sileshi, G. E. Trahey, and J. J. Dahl, Vasc. Med. **16**(4), 302–311 (2011).
[5]J. Rogowska, N. A. Patel, J. G. Fujimoto, and M. E. Brezinski, Heart **90**(5), 556–562 (2004).
[6]A. Migliori, J. L. Sarrao, W. M. Visscher, T. M. Bell, M. Lei, Z. Fisk, and R. G. Leisure, Physica B **183**(1–2), 1–24 (1993).
[7]M. Fatemi and J. F. Greenleaf, Science **280**(5360), 82–85 (1998).

[8]M. Muller, A. Sutin, R. Guyer, M. Talmant, P. Laugier, and P. A. Johnson, J. Acoust. Soc. Am. **118**(6), 3946–3952 (2005).
[9]L. Taeyong, C. Wen-Ming, L. Liang, S. S. Nathan, and B. P. Pereira, J. Biomech. **41**, S187–S187 (2008).
[10]T. Lee, R. S. Lakes, and A. Lal, Biomech. Model. Mechanobiol. **1**(2), 165–175 (2002).
[11]A. L. Oldenburg and S. A. Boppart, Phys. Med. Biol. **55**(4), 1189–1201 (2010).
[12]W. Qi, R. Chen, L. Chou, G. Liu, J. Zhang, Q. Zhou, and Z. Chen, J. Biomed. Opt. **17**(11), 110505 (2012).
[13]Y. C. Fung, *Biomechanics: Mechanical Properties of Living Tissues* (Springer, New York, 1993).
[14]X. Liang, A. L. Oldenburg, V. Crecea, E. J. Chaney, and S. A. Boppart, Opt. Express **16**(15), 11052–11065 (2008).
[15]C. Sun, B. Standish, and V. X. D. Yang, J. Biomed. Opt. **16**(4), 043001 (2011).